Analysis of Tsunami Propagation and Run-up with Upwind FVM

o Kim, Dae-Hong[1] / Cho, Yong-Sik[2] / Kim, Woo-Gu[3]

1. Introduction

Tsunamis are large water waves set in motion either by landslides, submarine volcanic explosions, or sea-bottom deformations associated with large submarine earthquakes. During last decades several devastating tsunamis have been occurred. These tsunamis not only killed many human beings but also caused serious property damages. Especially, nearshore tsunamis could cause severe coastal flooding and huge property damage. Therefore, a coastal inundation map based on the maximum run-up heights is essential to mitigate coastal casualties from unexpected nearshore tsunami attacks [*Liu et al.*, 1995].

In this paper, in order to investigate the run-up heights of nearshore tsunamis in the vicinity of a coastal area, a numerical model has been developed based on upwind finite volume method. The governing equations of the model are the nonlinear shallow-water equations. The governing equations are discretized explicitly by using finite volume method on unstructured grids. The numerical fluxes are reconstructed by TVD version of Weighted Averaged Flux (WAF) method. The computed numerical results have been verified by comparing to available analytic solutions and laboratory measurements. Good agreements have been observed.

2. Governing equations

As the tsunami approaches a coastal area, the wave length of the incident tsunami becomes shorter and the amplitude becomes larger as the leading wave of a tsunami propagates into shallower water. Therefore, the nonlinear convective inertia force and bottom friction terms become increasingly important, while the significance of the Coriolis force and the frequency dispersion terms diminishes.

Consequently, the nonlinear shallow-water equations in conservative form including bottom frictional effects are adequate to describe the flow motion in the coastal zone and can be written as follows:

$$\frac{\partial \mathbf{U}}{\partial t}+\frac{\partial \mathbf{E}}{\partial x}+\frac{\partial \mathbf{F}}{\partial y}=\mathbf{S} \tag{1}$$

In equation (1), the vector of conserved variables $\mathbf{U}$, the flux vectors $\mathbf{E}$ and $\mathbf{F}$ in the x- and y-directions and the source term $\mathbf{S}$ can be written as

$$\mathbf{U}=\begin{bmatrix} d \\ du \\ dv \end{bmatrix},\quad \mathbf{E}=\begin{bmatrix} du \\ du^2+\frac{1}{2}gd^2 \\ duv \end{bmatrix},\quad \mathbf{F}=\begin{bmatrix} dv \\ duv \\ dv^2+\frac{1}{2}gd^2 \end{bmatrix},\quad \mathbf{S}=\begin{bmatrix} 0 \\ gd(S_{ox}-S_{fx}) \\ gd(S_{oy}-S_{fy}) \end{bmatrix} \tag{2}$$

where d is the total water depth and u and v are the velocity components in the x- and y- directions, S_{ox} and S_{oy} are bed slope components, S_{fx} and S_{fy} are bottom friction terms in the x- and y- directions respectively, and g is the acceleration due to gravity.

---

1) Kim, Dae-Hong : Researcher, Water Resources Research Institute, KOWACO
2) Cho, Yong-Sik : Professor, Dept. of Civil Engineering, Hanyang University
3) Kim, Woo-Gu : Director General, Water Resources Research Institute, KOWACO

3. Numerical scheme

3.1 Finite volume method

The finite volume method (FVM) is an approach for dealing with a general unstructured grid. The major advantages of FVM are: an ability to use a flexible grid system, such as triangles or quadrilaterals suitable for more complex geometries, use of an integral conservation law, and a close relationship between a fractional step method and FVM.

By integrating the shallow-water equations (1) over an arbitrary cell, the basic equation of the FVM can be obtained as

$$\frac{\partial}{\partial t}\int_A \mathbf{U}dA + \oint_\Omega \mathbf{G}\cdot\mathbf{n}d\Omega = \oint_\Omega \mathbf{S}d\Omega \tag{3}$$

where $\mathbf{G}$ is the flux tensor, A and Ω are are the surface area and boundary of the control volume L, $\mathbf{n}$ is the outward unit vector normal to the boundary.

3.2 Reconstruction of flux using HLLC weighted averaged flux method

In equations (1), $\mathbf{U}$ is a vector of three conserved variables. In solving flux part, the solution to Riemann problem consists of three waves with speeds S separating four constant states as described in Fig. 1. Therefore the flux part of equation (1) is hyperbolic and the solution to Riemann problem consists of three waves with speeds equation (4).

$$\tilde{\mathbf{U}}(x,y)=\begin{cases}\mathbf{U}_L, & 0\le S_L & S_L=\min(u_L-\sqrt{gd_L},\ u_*-\sqrt{gd_*})\\ \mathbf{U}_L^*, & S_L\le 0\le S_* & S_*=u_*=\dfrac{u_L+u_R}{2}+\sqrt{gd_L}-\sqrt{gd_R}\\ \mathbf{U}_R^*, & S_*\le 0\le S_R & \\ \mathbf{U}_R, & S_R\le 0 & S_R=\max(u_R+\sqrt{gd_R},\ u_*+\sqrt{gd_*})\end{cases} \tag{4}$$

In second-order accurate WAF method, the flux is given as

$$\mathbf{E}_{i+1/2}=\frac{1}{2}(\mathbf{E}_i+\mathbf{E}_{i+1})-\frac{1}{2}\sum_{k=1}^{N}c_k\Delta\mathbf{E}^k_{i+1/2} \tag{5}$$

where c_k is the Courant number for a wave k of speed S_k and $\Delta\mathbf{E}^k_{i+1/2}=\mathbf{E}^{k+1}_{i+1/2}-\mathbf{E}^k_{i+1/2}$. As above mentioned, equation (5) is second-order and nonphysical oscillation can be created. Thus in order to control the numerical oscillation, the TVD scheme is employed like (6),

$$\mathbf{E}_{i+1/2}=\frac{1}{2}(\mathbf{E}_i+\mathbf{E}_{i+1})-\frac{1}{2}\sum_{k=1}^{N}sign(c_k)\varphi^k_{i+1/2}\Delta\mathbf{E}^k_{i+1/2} \tag{6}$$

where $\varphi^k_{i+1/2}$ is a WAF limiter function.

An advantage of HLLC approximate Riemann solver is that it uses wave speeds based on analytic dry front speeds, consequently, it produces better results than Roe's solver on dry bed. But wave speed estimeted by equation (4) assumes that there exists a finite water depth in the entire computational domain. If a dry bed exists on the left or right side of a cell then no shock exists and wave speeds should be estimated by ,

$$\begin{array}{ll}S_L=u_R-2\sqrt{gd_R} & S_L=u_L-\sqrt{gd_L}\\ S_*=S_L & S_*=S_R\\ S_R=u_R+\sqrt{gd_R}, & S_R=u_L+2\sqrt{gd_L}\end{array} \tag{7}$$

The source part can be solved by the fractional step method with an ordinary differential solver. In this study the source terms are solved by using explicit Euler method.

More details on numerical scheme is written on Kim et al (2002).

4. Numerical simulation and Discussion

4.1 Water Surface Oscillations in a Parabolic Basin

A two-dimensional moving boundary problem is tested on 400×400 cells and obtained predictions are compared with available analytical solutions. The bottom topography is described as $z_b = z_{bo}(1 - r^2/a^2)$ where r is the radius of the horizontal circular section of the paraboloid. The analytic solution is given as (Thacker, 1981)

$$h = z_{bo}\left[\frac{\sqrt{(1-A^2)}}{1-A\cos\omega t} - 1 - \frac{r^2}{a^2}\left\{\frac{1-A^2}{(1-a\cos\omega t)^2} - 1\right\}\right], \quad \omega = \frac{\sqrt{8gz_{bo}}}{a}, \quad A = \frac{(a^4 - r_o^4)}{(a^4 + r_o^4)} \tag{8}$$

where r_o=2500m, a=2000m, and z_{bo}=1.0m have been used.

The Figs. 4 show analytic and computed water surface elevations obtained at T=1/4 and T=2/4, in which T is the period of the fluid motion. Both models produce very good results, however the present model predicts more similar to the analytic solutions. From the results, it can be concluded that the computational and analytic solutions agree very well and the model is good for the application for moving boundary problem such as the prediction of flow which overflow bank, and the analysis of run-up and run-down process on a slope, and predictions of inundation.

4.2 Wave run-up and propagation around circular island

In order to verify the run-up heights of nearshore tsunami based on finite volume method, comparisons are made with experimental measurements of the run-up heights on the circular island at the CERC(Coastal Engineering Research Center). The basin was 30m wide and 25m long. The center of a circular island was located at x = 15m and y = 13m. Time histories of free surface displacements were measured at 27 different locations. Locations of wave gages are plotted in Figure 2. And the maximum run-up heights were measured with an interval of $\pi/8$ around a circular island. More detailed description on laboratory experiments including facilities can be found in *Liu et al.* [1995].

Figs. 5 present comparisons between wave gage data and numerical results. The simulation condition is that : e which is the ratio of solitary wave amplitute to still water depth. The still water depth is 0.032 m and the length of the wave generator is 27.432 m. Leading waves of numerical solutions are slightly stronger than frequency dispersion effects. Although some re-reflections are observed only in experimental data, overall agreement between experimental data and the numerical solutions is good.

The Fig. 3 presents the area of inundated by maximum run-up around the island for e=0.1 and the length of the wave generator is 27.432 m.

The agreement between experimental data and the numerical solutions by present model are good.

Acknowledgement

The second author was supported by research funds of the National Research Laboratory Program (Coastal Engineering Laboratory, Hanyang University).

References

Cho, Yong-Sik (1995). Numerical simulations of tsunami propagation and run-up, Ph.D. thesis, Cornell Univ., Ithaca, N.Y.

Kim, D. H., Kim, W. G. Chae, H. S. and Park, S. G. (2002). Development of 2D Dam Break Flow Analysis Model using Fractional Step Method, Water Engineering Research, Vol.3, No.1. 23-30

Liu, P.L.-F., Cho, Y.-S., Briggs, M.J., Kanoglu, U. and Synolakis, C.E. (1995). Run-up of solitary wave on a circular island, *J. Fluid Mech., 302,* 259-285

Thacker, W.C. (1981). Some exact solutions to the nonlinear shallow water wave equations. *J. of Fluid Mechanics,* 107, 499-508.

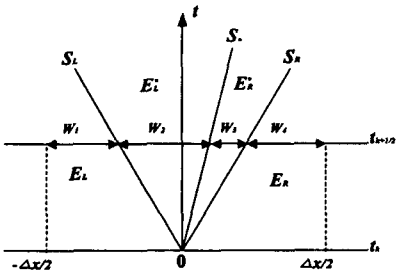

Fig. 1 Weights in WAF scheme

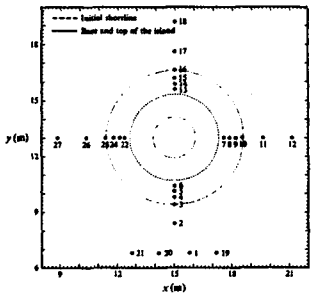

Fig. 2 Gage locations

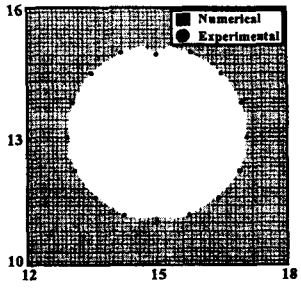

Fig. 3 Maximum run-up area

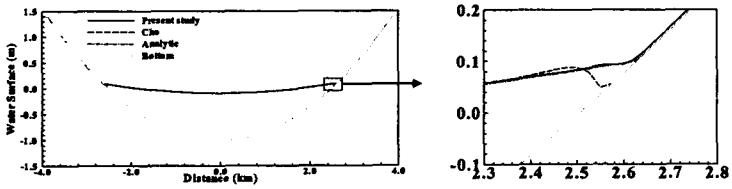

Fig. 4(a) Free surface profiles (T=1/4)

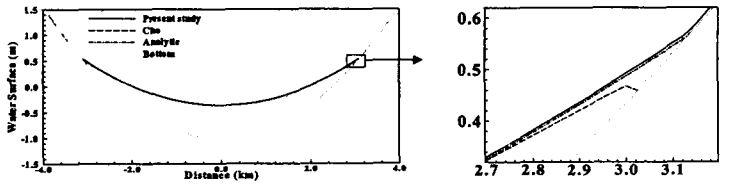

Fig. 4(b) Free surface profiles (T=2/4)

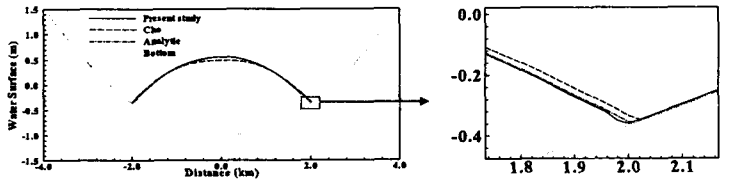

Fig. 4(c) Free surface profiles (T=4/4)

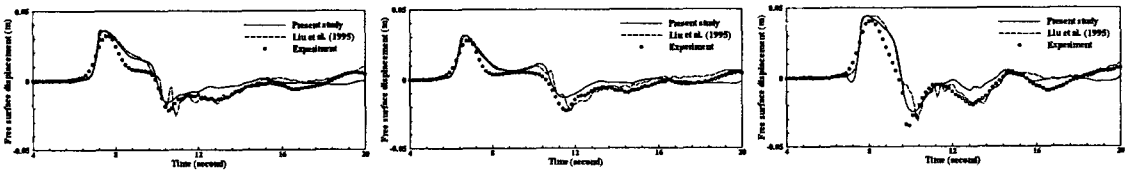

(a) Gage no. 2 (b) Gage no. 4 (3) Gage no. 6

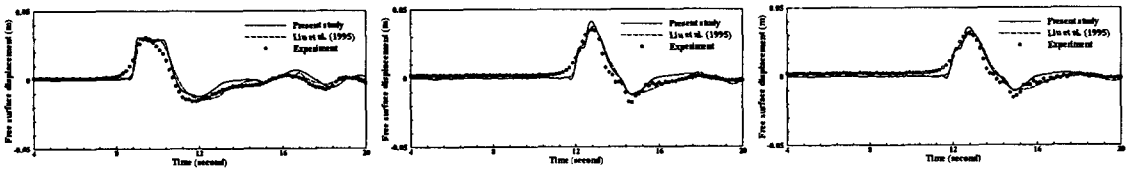

(d) Gage no. 8 (e) Gage no. 14 (f) Gage no. 15

Fig. 5. Comparisons between wave gage data and numerical results